PHOTONICS Research

Refractive index sensing based on a twisted nano-kirigami metasurface

Shuqi Qiao,[1,†] Xiaochen Zhang,[2,†] Qinghua Liang,[2] Yang Wang,[2] Chang-Yin Ji,[2] Xiaowei Li,[3] Lan Jiang,[3] Shuai Feng,[1] Honglian Guo,[1,4] and Jiafang Li[2,5]

[1]School of Science, Minzu University of China, Beijing 100081, China
[2]Key Laboratory of Advanced Optoelectronic Quantum Architecture and Measurement (Ministry of Education), Beijing Key Laboratory of Nanophotonics & Ultrafine Optoelectronic Systems, and School of Physics, Beijing Institute of Technology, Beijing 100081, China
[3]Laser Micro/Nano Fabrication Laboratory, School of Mechanical Engineering, Beijing Institute of Technology, Beijing 100081, China
[4]e-mail: hlguo@muc.edu.cn
[5]e-mail: jiafangli@bit.edu.cn
[†]These authors contributed equally to this work.

Received 12 October 2023; revised 19 November 2023; accepted 21 November 2023; posted 21 November 2023 (Doc. ID 507863); published 29 January 2024

Plasmonic sensing technology has attracted considerable attention for high sensitivity due to the ability to effectively localize and manipulate light. In this study, we demonstrate a refractive index (RI) sensing scheme based on open-loop twisted meta-molecule arrays using the versatile nano-kirigami principle. RI sensing has the features of a small footprint, flexible control, and simple preparation. By engineering the morphology of meta-molecules or the RI of the ambient medium, the chiral surface lattice resonances can be significantly enhanced, and the wavelength, intensity, and sign of circular dichroism (CD) can be flexibly tailored. Utilizing the relation between the wavelength of the CD peak and the RI of the superstrate, the RI sensor achieves a sensitivity of 1133 nm/RIU. Additionally, we analyze these chiroptical responses by performing electromagnetic multipolar decomposition and electric field distributions. Our study may serve as an ideal platform for applications of RI measurement and provide new insights into the manipulation of chiral light–matter interactions.

https://doi.org/10.1364/PRJ.507863

1. INTRODUCTION

Optical sensors utilize the interaction between the optical field and physical matters to generate an optical signal for sensing, which typically measure the wavelength, amplitude, and phase of light. Due to their properties of electrical passiveness, high sensitivity, freedom from electromagnetic interference, and wide dynamic range [1], optical sensors have been widely employed in the environment monitoring [2–4], analytical chemistry [5–7], biomedical diagnosis [8–12], and food processing industries [13–15]. Over the past decades, the development of industry and research has required sensors to be more compact and efficient [16,17], which promotes the exploration and development of new technologies and materials, especially plasmonic metamaterials.

With the development of micro-/nano-fabrication technology in recent years, strong localization and manipulation of light has been realized by using artificial plasmonic metamaterials. These plasmonic metamaterials break the diffraction limit of light and generate strong field enhancement, which induce versatile unique optical properties in wavefront conversion [18–20], polarization control [21–23], surface Raman scattering enhancement [24–26], discrimination of chiral molecules [27–29], photodetectors [30], etc. In particular, plasmon oscillations have a short penetration depth into the surrounding fluid, which makes them ideal for small and localized sensors in various biomedical applications [31–33]. In this aspect, researchers have explored various micro-/nano-structures for plasmonic sensing with high sensitivity to refractive index (RI) based on surface plasmon polariton or localized surface plasmon resonance (LSPR) mechanisms [34]. However, traditional spectroscopy measurements such as reflection and scattering may not be reliable for highly absorbing or complex biological media due to the signal noise [35]. A promising alternative is the use of circular dichroism (CD), which is insensitive to achiral absorbers or scatterers. By using CD, high signal-to-noise measurements are possible even in the presence of strong achiral absorbers [36]. Nevertheless, it remains challenging to fabricate chiral micro-/nano-structures to support strong chiral plasmon resonance and high sensitivity to surrounding media. On the one hand, strong chiroptical response generally requires preparation of the three-dimensional (3D) structures with high fabrication accuracy and uniformity. On the other hand, artificial micro-/nano-structures are usually located on the substrate, and the mismatch in RI between

the substrate and the surrounding media may affect the excitation of LSPR, thereby reducing the sensitivity. Therefore, it is necessary to develop an efficient and convenient plasmonic chiral structure and explore the impact of substrate on chiroptical responses to enhance sensing performance.

In this work, we propose and demonstrate an RI sensing scheme based on a chiral meta-molecule array fabricated by using a nano-kirigami method. The chiroptical response of the arrays under various geometric designs and environmental conditions is simulated and verified through experiments. By analyzing electric field distributions and scattering powers of various multipole moments, we realize the enhancement and reversal of CD excited by surface lattice resonances (SLRs) through the swing of the arms. Taking advantage of the high sensitivity of the CD spectrum of the meta-molecular array to the RI of the environment, we demonstrate a wavelength-modulated RI sensor, achieving the linear relationship between the resonant wavelength and RI of the superstrate with a sensitivity of 1133 nm/RIU. The experimental results show high linearity and are in good agreement with the simulations. Such a simple scheme could provide an important platform for ultra-miniaturization, high integration, multifunction, and high-speed optical sensing.

2. EXPERIMENTAL SECTION

A. Numerical Simulations

Numerical simulations were performed by using the finite element method on the COMSOL-Multiphysics platform. By adopting a bilayer stress distribution model, the conversion of two-dimensional (2D) patterns to 3D chiral meta-molecules was obtained. The optical transmissions were simulated under circularly polarized light (CPL) incidence that propagated along the z-axis direction. Perfectly matched layers on the top and bottom are set as absorbing boundary conditions. The periodic boundary conditions were applied to corresponding unit cells to realize hexagonal lattice copper arrays in the x–y plane.

B. Sample Fabrications

The meta-molecule array without substrate was fabricated by using the focused ion beam (FIB)-based nano-kirigami method on gold nano-films suspended on the copper grid [37]. The nano-kirigami method includes a two-dosage ion beam irradiation, which was implemented by employing the same FIB facility (FEI Helios 600i) in a one-step and on-site fabrication process. First, the suspended gold thin film on a copper grid mesh was etched by a high-dose ion beam (>600 pC/μm^2), resulting in the arms attached to the edge of round holes. Second, by utilizing the irradiation-induced stress, the arms were deformed and twisted by the frame scanning method with a relatively low dose (≈10 to 40 pC/μm^2), i.e., the global ion beam irradiation. The whole fabrication process was less than 30 min for an array of 306 units.

The fabrication of nano-kirigami meta-molecules used silica substrate coated with a 60-nm-thick gold film. First, the gold film was etched by FIB with a high-dose ion beam (>600 pC/μm^2). After a careful wet etching process with hydrofluoric acid (with the concentration of 8%), the silica substrate beneath the etched areas was eroded while the other parts of the silica remained unchanged due to the slow etching. In such a way, the 2D arms were locally suspended. Finally, the suspended arms were deformed by global irradiation with a low-dose ion beam (≈10 to 40 pC/μm^2) and the 3D meta-molecule arrays were formed. In the RI sensing experiment, the refractive index liquids (Cargille) with different RIs were dropped on the sample to achieve the change of the superstrate RI.

During the above fabrication process, the acceleration voltage and beam current of Ga^+ were set at 30 kV and 24 pA, respectively. For the meta-molecule array, the lattice period was designed to be 1.4 μm and the size of sample area was ~25 μm × 25 μm.

C. Optical Characterizations

A home-built optical system was utilized to measure the transmission spectra. The supercontinuum light sources (SC-Pro, YSL) with a repetition rate of 5 MHz were collimated before passing through a linear polarizer (650–2000 nm, Thorlabs, LPNIR100-MP2) and a quarter-wave plate (1100–2000 nm, Thorlabs, AQWP10M-1600) to obtain circularly polarized light. An objective lens (10× with numerical aperture NA = 0.3, Olympus, LMPlan) was used to focus the incident light onto the sample. Another infrared objective lens (10× with NA 0.3, Olympus, UPlanFL) was used to collect the transmitted signals which were subsequently delivered to a spectrometer (1000 to 2200 nm, Ocean Optics, NIRQuest). Meanwhile, a CCD camera (MER-500-14U3C-L, Daheng Imaging) was placed in a switchable optical path for imaging.

3. RESULTS AND DISCUSSION

A. Structural Designs

Here the structures are designed based on a nano-kirigami method, which is an *in situ* and large-area preparation method by combining high-dose FIB etching and low-dose FIB buckling [37]. With the unique feature of 3D twisting, the nano-kirigami method is highly desirable for the fabrication of chiral nano-structures. Different from the previous closed-loop structures with slits in the gold film, here an open-loop structure with three arms is designed (Fig. 1). As illustrated in Fig. 1(a), the arms can swing around the connection points by adjusting angle φ. The Freeth's Nephroid spiral curve is selected to construct the arms, whose polar equation is $\rho = a[1 + 2\ \sin(\theta/2)]$ with the unit of micrometers. In our design, the value of the parameter a is 0.162 and the lattice period is 1.2 μm. By choosing θ_1 and θ_2, we can determine where the curve starts and ends. For the quantitative evaluation of the chiral effects of meta-molecules, CD denotes the differential absorption between left circular polarization (LCP) light and right circular polarization (RCP) light in the interaction with chiral substances, which is defined as $\mathrm{CD} = A_{\mathrm{RCP}} - A_{\mathrm{LCP}}$, where A_{RCP} and A_{LCP} denote the absorptions for RCP and LCP incidences, respectively [38]. Due to the C_3 symmetry of the structure, the reflections under the normal incidences of LCP light and RCP light are identical. Therefore, the value of CD can also be calculated using the formula of $\mathrm{CD} = T_{\mathrm{LCP}} - T_{\mathrm{RCP}}$, where T_{LCP} and T_{RCP} denote the transmissions for LCP and RCP incidences, respectively.

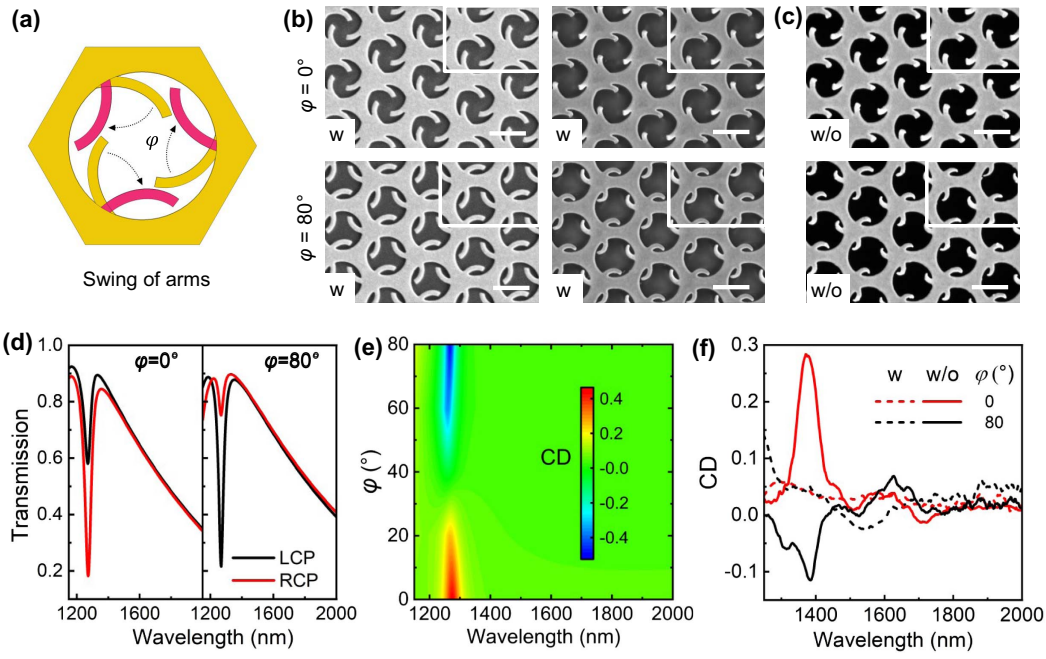

Fig. 1. Design of the open-loop twisted meta-molecule arrays. (a) Schematic diagram of the 2D meta-molecule with three arms which can be swung by an angle φ. (b) Top-view and side-view (insets) SEM images of the fabricated 2D and 3D meta-molecule arrays on the silica substrate (w). (c) Top-view and side-view SEM images of the fabricated free-standing 3D meta-molecule arrays without the substrate (w/o). (d) Simulated LCP and RCP transmission spectra of the two meta-molecule arrays without the silica substrate. (e) Calculated CD spectra versus the wavelength and φ. (f) Measured CD spectra of the meta-molecule arrays with and without the substrate. The lattice periods of simulated and experimental arrays are 1.2 and 1.4 μm, respectively. Scale bars: 1 μm.

The proposed meta-molecule arrays with $\varphi = 0°$ and $\varphi = 80°$ in Fig. 1(a) are scaled-up and fabricated with (w) and without (w/o) the silica substrate. The 2D meta-molecules arranged in a hexagonal lattice are transformed into 3D twisted meta-molecules through the FIB-based nano-kirigami method, as demonstrated in Figs. 1(b) and 1(c). These open-loop structures offer several advantages, including a small footprint, flexible control, easy preparation, and intriguing chiroptical response, making them promising for further applications in micro-/nano-electromechanical systems and optical sensors.

B. CD Engineering by Swinging the Arms

We first simulate the effect of φ on CD response in the open-loop structures without the substrate. As Figs. 1(b) and 1(c) show, the arms can swing around the connection points with φ increasing from 0° to 80°. As plotted in Fig. 1(d), the transmission of LCP light is larger than that of RCP light at resonance wavelength when $\varphi = 0°$, while such a situation has been reversed for the case of $\varphi = 80°$. The simulated CD spectra versus wavelength and φ in Fig. 1(e) clearly show the dramatic CD reversal near the wavelength of the lattice period. A positive CD with a value of +0.40 evolved into a negative CD of −0.54. The experimental measurement results of the solid lines in Fig. 1(f) also demonstrate this chiral inversion. Specifically, the CD is almost zero when the swing angle φ is about 40°. Overall, the value of CD will gradually increase as the arms approach the edge of the unit cell and decrease as the arms approach the center.

Such CD reversal can be verified by the normalized electric field distributions at corresponding resonance wavelengths, as plotted in Figs. 2(a) and 2(b). In the case of $\varphi = 0°$, the light–matter interaction under the LCP light incidence is weaker than that under the RCP light incidence at the resonance wavelengths, which denotes a smaller absorption, i.e., a larger transmission of LCP light, resulting in a positive value of CD. In comparison, the case is contrary when $\varphi = 80°$. This switch of the CD sign can be explained by the changes in geometrical chirality during swinging. To prove this visually, we imitate the twisted meta-molecules with $\varphi = 0°, 40°$, and 80° [Fig. 2(c)] and design straight meta-molecules composed of out-of-plane inclined columns and nano-hole arrays [Fig. 2(d)], in which the straight meta-molecules with $\varphi = 0°$ and 80° are enantiomers. With the creation of meta-molecules with opposite chirality, symmetrical CD spectra are obtained, as shown in Fig. 2(e). More fascinatingly, the calculated CD reversal of the straight meta-molecules bearing a close resemblance to the diagram of the twisted meta-molecules, unambiguously testifies that the reason for CD reversal by the swing of arms is the inversion of structural chirality.

As for general geometries, mirror inversion is always challenging in the experimental process. Here, the mirror image of the meta-molecules effortlessly takes shape through the swing of arms, bringing about a dramatic change of chiroptical response. Compared with traditional mirror geometries, the scheme of nano-kirigami provides a novel mechanism to reverse structural chirality for highly dynamic manipulation of chiroptical properties.

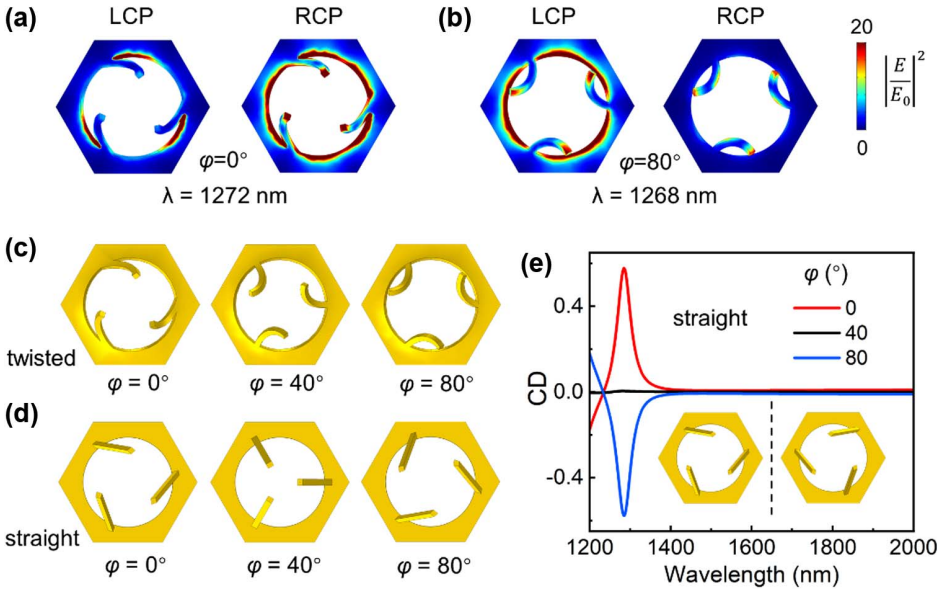

Fig. 2. Analysis of the CD reversal. (a), (b) Top-view electric field distributions of the meta-molecule surfaces for $\varphi = 0°$ (at $\lambda = 1272$ nm) and $\varphi = 80°$ (at $\lambda = 1268$ nm) under the normal RCP and LCP light incidence. (c) Schematic diagram of the deformed twisted meta-molecules with $\varphi = 0°$, $\varphi = 40°$, and $\varphi = 80°$. (d) Schematic diagram of the straight meta-molecules with $\varphi = 0°$, $\varphi = 40°$, and $\varphi = 80°$. (e) Calculated CD spectra of straight meta-molecules in (d). Inset: top view of the meta-molecules. Here, the lattice period is 1.2 μm.

C. Experimental Exploration of the Environmental Sensitivity of Chiral Response

For experimental demonstrations, the proposed meta-molecule arrays with $\varphi = 0°$ and $\varphi = 80°$ in Fig. 1(a) are fabricated. The lattice period is chosen to be 1.4 μm to minimize the fabrication imperfections, ensuring the validity of the revealed physical mechanisms. Generally, the existence of a substrate can greatly improve the integration of the nano-kirigami metasurface. However, the asymmetric dielectric environment around the meta-molecules can significantly suppress the chiral SLRs. To investigate the effect of the substrate on SLR excitation, we prepare samples on both suspended gold film and silica substrate, respectively.

As the scanning electron microscopy (SEM) images shown in Fig. 1(b), the 2D precursors are initially fabricated on a gold film situated on the silica substrate using high-dose FIB irradiation. After wet etching, the 3D chiral meta-molecule array with a deformation height of about 450 nm is realized by employing low-dose global FIB irradiations. Meanwhile, the suspended 3D chiral meta-molecule array without the silica substrate is fabricated via high-dose and subsequently low-dose FIB irradiation, as shown in Fig. 1(c) (see more experimental details in Section 2).

The CD spectra of the fabricated 3D chiral arrays under the normal CPL incidence are characterized by a home-built optical system, as shown in Fig. 1(f). To quantitatively characterize CD reversal, the CD spectra of the 3D chiral meta-molecule arrays without the silica substrate are shown in the solid lines. It can be seen that the positive CD peak and negative CD dip with the values of 0.28 and –0.11 are experimentally achieved for $\varphi = 0°$ and $\varphi = 80°$, respectively. Although the measured transmission spectra are slightly weaker than the simulated ones, the fascinating CD reversal is successfully achieved in the experiments. The difference is mainly caused by the implantations of Ga^+ ions during FIB irradiations. The CD spectrum with the silica substrate is shown as the dashed lines, which specially shows that the CD intensity decreases sharply in the presence of an asymmetric environment. Thus, the experimental observation provides solid evidence of the effect of an asymmetric environment on chiral SLRs.

D. Effect of RI of the Environmental Medium on CD Response

We chose the meta-molecule array with a lattice period of 1.4 μm and a φ of 0° (Fig. 1) for further investigation on the effect of environmental RI on CD. We conduct simulations of CD spectra under two environmental conditions: symmetric RI and asymmetric RI. The transmission spectrum measurement model of the meta-molecule array uses the COMSOL-Multiphysics platform, in which n_{sup} represents the RI of the superstrate and n_{sub} is the RI of the substrate. For the case of symmetric RI, we choose $n_{sup} = n_{sub}$ to ensure that the suspended meta-molecule array is in a uniform medium. For the case of asymmetric RI, n_{sub} is kept constant as the RI of silica of 1.45, and n_{sup} gradually approaches n_{sub} from 1. Three pairs of periodic boundary conditions are applied on the unit cell to simulate a hexagonal lattice array. A 3D gold meta-molecule sits on a silica substrate. Perfectly matched layers at the top and bottom ensure that outgoing waves from the interior of the computational region are all absorbed and not reflected back into the interior. The transmission under circularly polarized light incidence is monitored by the output port, which varies with the RI of the environment.

As shown in Fig. 3(a), under the symmetric environment, the peak intensity of CD can be kept close to 0.6 with the RI change, which indicates that the chiral SLRs are not suppressed

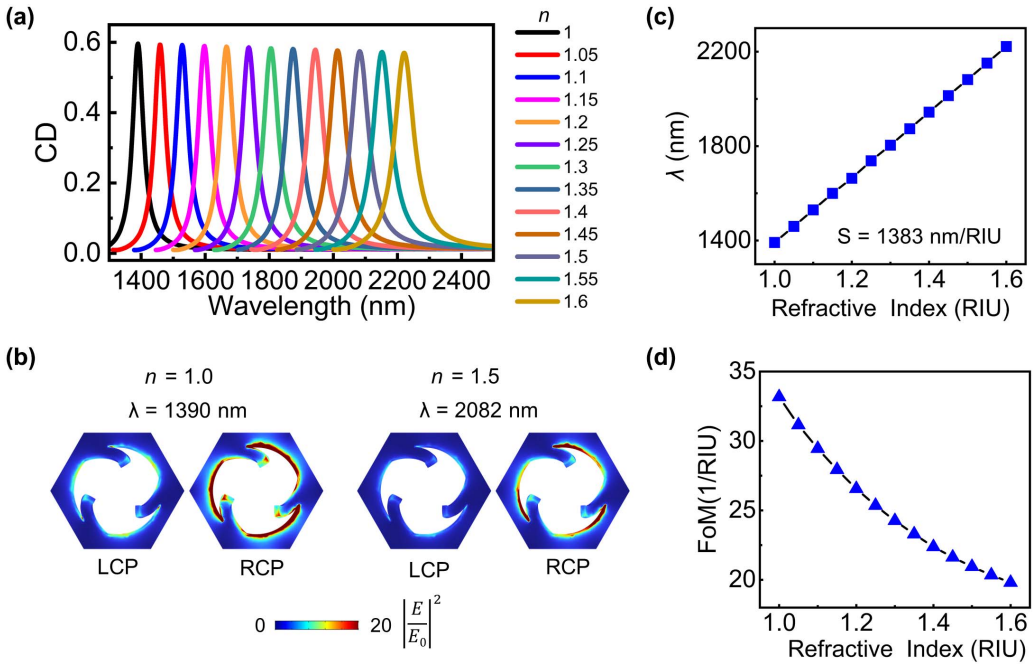

Fig. 3. Effect of RI of the symmetrical environmental medium on CD response. (a) CD spectra with different RIs of the environment. (b) Top-view electric field distributions of the meta-molecule surfaces for $n = 1.0$ (at $\lambda = 1390$ nm) and $n = 1.5$ (at $\lambda = 2082$ nm) under the normal RCP and LCP light incidence. (c) Simulated resonance wavelength versus the RI of the environment. (d) Simulated FoM under different RIs of the environment. Here, the lattice period is 1.4 μm.

in the environment of symmetric RI. The normalized surface electric field distributions at the corresponding wavelengths of CD peaks are shown in Fig. 3(b). Apparently, the intensity of the electric field excited by RCP light is greater than that of LCP light in the case of symmetric RIs of both 1 and 1.5, which denotes larger absorption and smaller transmission of RCP light, resulting in strong positive CD peaks. Figure 3(c) shows the linear relationship between the wavelength of the CD peak and RI, in which the wavelength of the CD peak increases from 1400 nm to 2200 nm as the RI increases from 1 to 1.6. The RI sensitivity is defined as $S_{\mathrm{RI}} = \frac{\Delta\lambda}{\Delta n}$, which is calculated to be 1383 nm/RIU. The figure of merit (FoM) is used to normalize the S_{RI} and describe how precise we can measure the resonance peak, which is calculated as $\mathrm{FoM} = \frac{S_{\mathrm{RI}}}{\mathrm{FWHM}}$. FWHM is short for the full width at half-maximum. As shown in Fig. 3(d), the FoM gradually decreases with the increase of RI, which attributes to the fact that the CD peaks are sharper when the RI of the environment is smaller [see Fig. 3(a)].

Samples with the substrate are more convenient for the subsequent processing and packaging of devices. Therefore, the impact of environmental RI on the resonance of meta-molecular arrays on a silica substrate is investigated for further applications. As for asymmetric RI, we simulate the CD spectra with varying n_{sup} and constant n_{sub} in Fig. 4(a). We can clearly see that when the difference between n_{sup} and n_{sub} ($n_{\mathrm{sup}} = 1$, $n_{\mathrm{sub}} = 1.45$) reaches its maximum, the resonance is suppressed due to the asymmetry of the environment, resulting in weak CD. As n_{sup} increases ($1 < n_{\mathrm{sup}} < 1.2$), the asymmetry of the environment gets weak, and the value of CD peak increases significantly. When n_{sup} increases to 1.2, a CD peak with the value of 0.5 appears. When n_{sup} further approaches the RI of the silica substrate ($1.25 \le n_{\mathrm{sup}} \le 1.6$), the amplitude of the CD peak begins to increase slightly and the optical chiral response keeps giant; meanwhile the resonance wavelength is red-shifted in a linear way. From the CD spectra, we can intuitively see the inhibition effect of the asymmetric RI environment on chiral SLRs, which can be further revealed by comparing the normalized surface electric field distributions in Fig. 4(b). The intensity of the electric field excited by both RCP and LCP light in the case of $n_{\mathrm{sup}} = 1$ is low, which reflects a very weak light–matter interaction, resulting in a weak CD, while the intensity of the electric field excited by RCP light is greater than that of LCP light in the case of $n_{\mathrm{sup}} = 1.5$. The obviously enhanced plasmon resonance mode resulted in a sharp CD peak. The sensitivity of wavelength shift to unit RI is calculated in Fig. 4(c), which is 1133 nm/RIU. As shown in Fig. 4(d), the FoM in the asymmetric RI environment decreases continuously as well as that in the symmetric RI environment.

E. Design of the RI Sensor

The variation of the n_{sup} within a certain range causes the linear shift of the resonant wavelength, that is, the change of the n_{sup} is converted into the change of the optical signal. This effect can be utilized in RI sensors for precise and sensitive measurements. For further experimental verification, the effect of the RI of the environment on CD response is investigated.

As shown in Fig. 5(a), the RI sensing experiments were conducted by putting refractive index liquids with n_{oil} of 1.3 to 1.45 on the silica-substrate-based meta-molecule array. Specifically, the 3D twisted meta-molecule arrays were first milled in a gold film by high-dose FIB lithography, followed

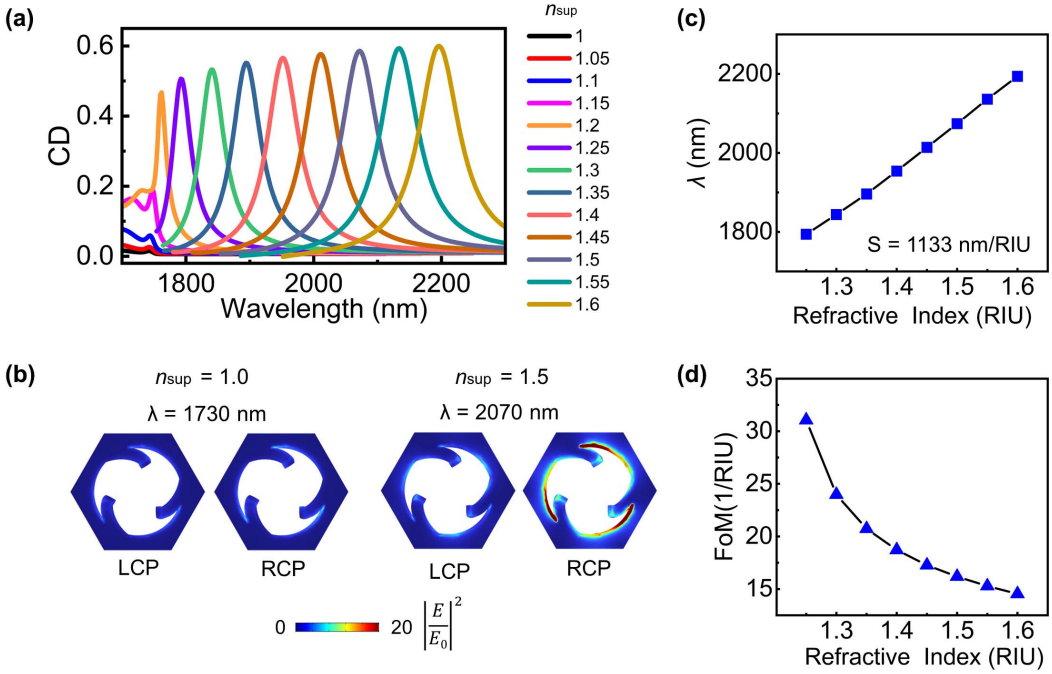

Fig. 4. Effect of RIs of the unsymmetrical environmental medium on CD responses. (a) CD spectra with different n_{sup}. (b) Top-view electric field distributions of the meta-molecule surfaces for $n_{sup} = 1.0$ (at $\lambda = 1730$ nm) and $n_{sup} = 1.5$ (at $\lambda = 2070$ nm) under the normal RCP and LCP light incidence. (c) Simulated resonance wavelength versus n_{sup}. (d) Simulated FoM with different n_{sup}. The lattice period is 1.4 μm.

by a wet etching process and low-dose FIB irradiation. In order to show the twisted structure more clearly, the large-area SEM images are displayed in Figs. 5(b) and 5(c). After the fabrication of the sample, a droplet of refractive index liquid was dropped onto the 3D twisted meta-molecule array and covered by a cover slip. The optical transmission spectra were measured under static environments. After each measurement, the sample was cleaned with acetone solution and the above steps were repeated until CD measurements with all refractive index liquid were completed. It is found that the meta-molecule array can maintain a stable state during the different measurements, as also verified by the consistency between simulation and experimental results. Additionally, the open-loop geometry is easier for the fabrication of smaller nano-structures, as well as for the solution to penetrate into the gap between the kirigami structure and the silica substrate, which results in a relatively uniform RI environment that facilitates the rising of the CD responses, as demonstrated in both Figs. 1(f) and 3(a). Consequently, the study of nano-kirigami metasurfaces is extended from the exploration of the intrinsic properties to the applications in detecting the external interactions. As shown in Figs. 5(d) and 5(e), the measured resonance wavelengths show obvious linear redshift with the increase of n_{oil}, which is consistent with the simulation results. The relationship between resonance wavelength and RI is plotted in Fig. 5(f), in which the experimental and simulated sensitivity of the RI sensor, $\Delta\lambda/\Delta n$, is calculated to be 1133 nm/RIU. The corresponding measured FoM value is ~18 when $n_{oil} = 1.3$ and decreases to ~7 when $n_{oil} = 1.45$, the trend of which is also consistent with the theoretical prediction in Fig. 4(d).

It should be mentioned that planar 2D metasurfaces normally have weak CD response due to the in-plane mirror symmetry, making them less competitive for the RI sensing of CD signals. In comparison, the nano-kirigami metasurfaces designed here have an out-of-plane twist that breaks the mirror symmetry, which will produce a strong CD response. As the simulation results show in Fig. 5(g), the optical CD response of the 2D planar precursors is difficult to be identified, while the 3D deformed metasurfaces have sharp CD peaks, and the greater the degree of arm deformation, the larger the CD peak value. Such enhanced CD responses in more deformed 3D configurations are helpful to increase the CD signal-to-noise ratio and thus enhance the sensing performance, although the linear sensitivity of the sensor changes little when the height changes from 250 to 400 nm [Fig. 5(f)]. It is worth mentioning that due to the flexibility of the structural design, the sensitivity of the RI sensor can be further improved by changing the structural parameters, such as the length, curvature, and rotation angle of the arms.

4. CONCLUSION

In this paper, we proposed and demonstrated an RI sensing scheme based on a chiral meta-molecule array fabricated by using a nano-kirigami method. By swinging the arms, a remarkable reversal and enhancement of chiroptical response near the wavelength of the lattice period have been realized. Further analysis of the electric field and the electromagnetic multipolar decomposition was explored in detail to reveal the profound mechanism of the chiroptical response. Meanwhile, we have investigated the effect of ambient RI on the chiroptical response

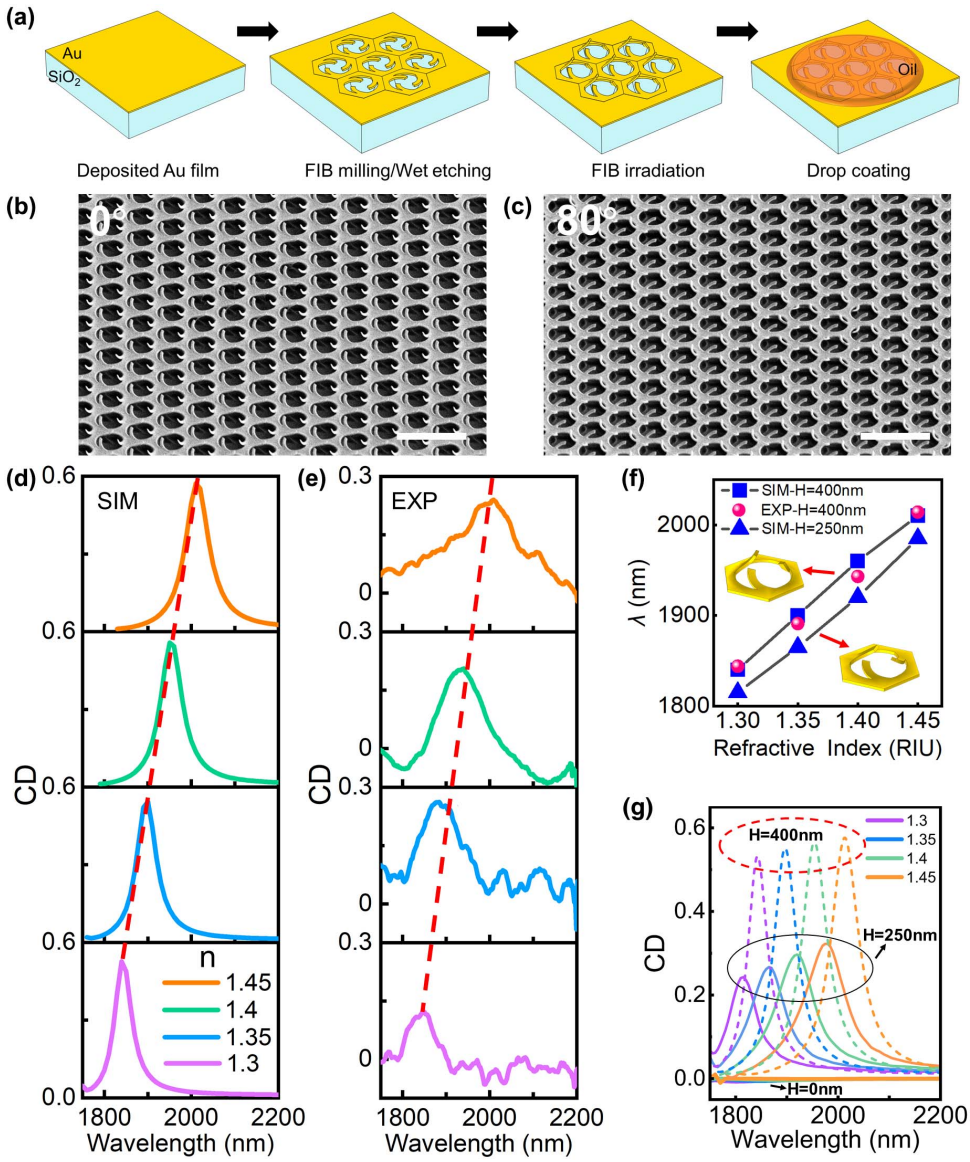

Fig. 5. Experimental demonstrations of the RI sensing. (a) Schematic diagram of the experimental flow of RI sensing. (b), (c) Side-view SEM images of the 3D arrays after global irradiation. The lattice period is 1.4 μm. Scale bars: 2.5 μm. (d), (e) Simulated and measured CD spectra with refractive index liquids of different RIs. (f) Simulated and measured resonance wavelength versus the RI of the refractive index liquids with meta-molecules of $H = 250$ and 400 nm, respectively. (g) Simulated CD response of meta-molecule array with different heights. The CD spectra of $H = 0$, 250, and 400 nm are denoted by solid thick lines, solid thin lines, and dashed lines, respectively.

by comparing the CD spectra of the meta-molecule arrays with or without a substrate. Based on these findings, an NIR wavelength-regulated RI sensor has been achieved with a sensitivity of 1133 nm/RIU. Such an efficient tailoring of the chiral open-loop nano-geometries and the corresponding CD response not only provides a new way to manipulate the light–matter interaction, but also creates a promising platform for deformable nano-kirigami structures in the areas of optical sensing applications.

Funding. Beijing Municipal Science and Technology Commission, Administrative Commission of Zhongguancun Science Park (Z211100004821009); Beijing Municipal Natural Science Foundation (1212013, Z190006); National Natural Science Foundation of China (12074446, 61975016, 12204041, T2325005, 62375016); Science and Technology Project of Guangdong (2020B010190001); China Postdoctoral Science Foundation (2021M700436).

Acknowledgment. The authors thank the Analysis and Testing Center from BIT for assistance in facility support.

Disclosures. The authors declare no conflicts of interest.

Data Availability. All the data supporting the findings of this study are available within the paper, or from the corresponding authors upon reasonable request.

REFERENCES

1. V. K. Rai, "Temperature sensors and optical sensors," Appl. Phys. B **88**, 297–303 (2007).
2. B. Liu, J. Zhuang, and G. Wei, "Recent advances in the design of colorimetric sensors for environmental monitoring," Environ. Sci. Nano **7**, 2195–2213 (2020).
3. M. B. Stuart, A. J. McGonigle, and J. R. Willmott, "Hyperspectral imaging in environmental monitoring: a review of recent developments and technological advances in compact field deployable systems," Sensors **19**, 3071 (2019).
4. R. Min, Z. Liu, L. Pereira, *et al.*, "Optical fiber sensing for marine environment and marine structural health monitoring: a review," Opt. Laser Technol. **140**, 107082 (2021).
5. J. Chen, Y. Huang, P. Kannan, *et al.*, "Flexible and adhesive surface enhance Raman scattering active tape for rapid detection of pesticide residues in fruits and vegetables," Anal. Chem. **88**, 2149–2155 (2016).
6. Z. Hai, J. Li, J. Wu, *et al.*, "Alkaline phosphatase-triggered simultaneous hydrogelation and chemiluminescence," J. Am. Chem. Soc. **139**, 1041–1044 (2017).
7. J. Wackerlig and R. Schirhagl, "Applications of molecularly imprinted polymer nanoparticles and their advances toward industrial use: a review," Anal. Chem. **88**, 250–261 (2016).
8. E. Morales-Narváez, H. Golmohammadi, T. Naghdi, *et al.*, "Nanopaper as an optical sensing platform," ACS Nano **9**, 7296–7305 (2015).
9. A. Dhiman, P. Kalra, V. Bansal, *et al.*, "Aptamer-based point-of-care diagnostic platforms," Sens. Actuators B **246**, 535–553 (2017).
10. S. M. Mousavi, M. Zarei, S. A. Hashemi, *et al.*, "Gold nanostars-diagnosis, bioimaging and biomedical applications," Drug Metabol. Rev. **52**, 299–318 (2020).
11. K. Nejati, M. Dadashpour, T. Gharibi, *et al.*, "Biomedical applications of functionalized gold nanoparticles: a review," J. Cluster Sci. **33**, 1–16 (2022).
12. J. Guo, C. Yang, Q. Dai, *et al.*, "Soft and stretchable polymeric optical waveguide-based sensors for wearable and biomedical applications," Sensors **19**, 3771 (2019).
13. H. Ouyang, X. Tu, Z. Fu, *et al.*, "Colorimetric and chemiluminescent dual-readout immunochromatographic assay for detection of pesticide residues utilizing g-C_3N_4/$BiFeO_3$ nanocomposites," Biosens. Bioelectron. **106**, 43–49 (2018).
14. J. Ma, D.-W. Sun, H. Pu, *et al.*, "Advanced techniques for hyperspectral imaging in the food industry: principles and recent applications," Ann. Rev. Food Sci. Technol. **10**, 197–220 (2019).
15. L. Rodriguez-Saona, D. P. Aykas, K. R. Borba, *et al.*, "Miniaturization of optical sensors and their potential for high-throughput screening of foods," Curr. Opin. Food Sci. **31**, 136–150 (2020).
16. Z.-B. Fan, H.-Y. Qiu, H.-L. Zhang, *et al.*, "A broadband achromatic metalens array for integral imaging in the visible," Light Sci. Appl. **8**, 67 (2019).
17. S. Gwo and C.-K. Shih, "Semiconductor plasmonic nanolasers: current status and perspectives," Rep. Prog. Phys. **79**, 086501 (2016).
18. Q. Song, M. Odeh, J. Zúñiga-Pérez, *et al.*, "Plasmonic topological metasurface by encircling an exceptional point," Science **373**, 1133–1137 (2021).
19. F. Ding, Y. Chen, and S. I. Bozhevolnyi, "Focused vortex-beam generation using gap-surface plasmon metasurfaces," Nanophotonics **9**, 371–378 (2020).
20. F. Ding, Y. Chen, and S. I. Bozhevolnyi, "Gap-surface plasmon metasurfaces for linear-polarization conversion, focusing, and beam splitting," Photonics Res. **8**, 707–714 (2020).
21. Q. Tan, Z. Xu, D. H. Zhang, *et al.*, "Polarization-controlled plasmonic structured illumination," Nano Lett. **20**, 2602–2608 (2020).
22. A. C. Tasolamprou, E. Skoulas, G. Perrakis, *et al.*, "Highly ordered laser imprinted plasmonic metasurfaces for polarization sensitive perfect absorption," Sci. Rep. **12**, 19769 (2022).
23. J. Jin, X. Li, Y. Guo, *et al.*, "Polarization-controlled unidirectional excitation of surface plasmon polaritons utilizing catenary apertures," Nanoscale **11**, 3952–3957 (2019).
24. X. Wang, S.-C. Huang, S. Hu, *et al.*, "Fundamental understanding and applications of plasmon-enhanced Raman spectroscopy," Nat. Rev. Phys. **2**, 253–271 (2020).
25. X. X. Han, R. S. Rodriguez, C. L. Haynes, *et al.*, "Surface-enhanced Raman spectroscopy," Nat. Rev. Methods Primers **1**, 87 (2022).
26. J. E. Park, N. Yonet-Tanyeri, E. V. Ende, *et al.*, "Plasmonic microneedle arrays for *in situ* sensing with surface-enhanced Raman spectroscopy (SERS)," Nano Lett. **19**, 6862–6868 (2019).
27. Y. Chen, W. Du, Q. Zhang, *et al.*, "Multidimensional nanoscopic chiroptics," Nat. Rev. Phys. **4**, 113–124 (2022).
28. Y. Chen, W. Chen, X. Kong, *et al.*, "Can weak chirality induce strong coupling between resonant states?" Phys. Rev. Lett. **128**, 146102 (2022).
29. Y. Chen, C. Zhao, Y. Zhang, *et al.*, "Integrated molar chiral sensing based on high-*Q* metasurface," Nano Lett. **20**, 8696–8703 (2020).
30. Z. Yin, X. Hu, J. Zeng, *et al.*, "Self-powered circularly polarized light detector based on asymmetric chiral metamaterials," J. Semicond. **41**, 122301 (2020).
31. Y. Ziai, F. Petronella, C. Rinoldi, *et al.*, "Chameleon-inspired multifunctional plasmonic nanoplatforms for biosensing applications," NPG Asia Mater. **14**, 18 (2022).
32. E. Elliott, K. Bedingfield, J. Huang, *et al.*, "Fingerprinting the hidden facets of plasmonic nanocavities," ACS Photonics **9**, 2643–2651 (2022).
33. H. Ye, C. Nowak, Y. Liu, *et al.*, "Plasmonic LAMP: improving the detection specificity and sensitivity for SARS-CoV-2 by plasmonic sensing of isothermally amplified nucleic acids," Small **18**, 2107832 (2022).
34. Y. Xu, P. Bai, X. Zhou, *et al.*, "Optical refractive index sensors with plasmonic and photonic structures: promising and inconvenient truth," Adv. Opt. Mater. **7**, 1801433 (2019).
35. H.-H. Jeong, A. G. Mark, T.-C. Lee, *et al.*, "Active nanorheology with plasmonics," Nano Lett. **16**, 4887–4894 (2016).
36. X. Duan, S. Kamin, F. Sterl, *et al.*, "Hydrogen-regulated chiral nanoplasmonics," Nano Lett. **16**, 1462–1466 (2016).
37. J. Li and Z. Liu, "Focused-ion-beam-based nano-kirigami: from art to photonics," Nanophotonics **7**, 1637–1650 (2018).
38. J. T. Collins, C. Kuppe, D. C. Hooper, *et al.*, "Chirality and chiroptical effects in metal nanostructures: fundamentals and current trends," Adv. Opt. Mater. **5**, 1700182 (2017).